

Electronic Supplementary Information

Selective Electrochemical Reduction of Carbon Dioxide to Formic Acid Using Indium-Zinc Bimetallic Nanocrystals

Ik Seon Kwon,^{†a} Tekalign Terfa Debela,^{†b} In Hye Kwak,^{†a} Hee Won Seo,^{†a} Kidong Park,^a
Doyeon Kim,^a Seung Jo Yoo,^c Jin-Gyu Kim,^c Jeunghye Park,^{*a} and Hong Seok Kang^{*d}

^a Department of Chemistry, Korea University, Sejong 339-700, Republic of Korea; E-mail address: parkjh@korea.ac.kr;

^b Institute for Application of Advanced Materials, Jeonju University, Chonju, Chonbuk 55069, Republic of Korea

^c Division of Electron Microscopic Research, Korea Basic Science Institute, Daejeon 305-806, Republic of Korea.

^d Department of Nano and Advanced Materials, College of Engineering, Jeonju University, Chonju, Chonbuk 55069, Republic of Korea; E-mail address: hsk@jj.ac.kr

[†]I. S. Kwon, T. T. Debela, I. H. Kwak, and H. W. Seo equally contribute as the first author.

Contents

I. Experimental Section

II. Supplementary Table

Table S1. Comparison of CRR catalytic efficiency of In-based catalysts.

III. Supplementary Figures

Figure S1. XRD pattern of Zn_{1-x}In_xO NCs.

Figure S2. TEM images of Zn_{1-x}In_xO NCs.

Figure S3. XPS survey and fine-scanned spectrum of Zn_{1-x}In_xO NCs.

Figure S4. XANES and EXAFS spectrum of Zn_{1-x}In_xO NCs.

Figure S5. Current density during the pre-reduction step.

Figure S6. XRD pattern of $Zn_{1-x}In_x$ NCs.

Figure S7. Nyquist plots.

Figure S8. Cyclic voltammograms for evaluation of double-layer capacitance.

Figure S9. TEM images of $Zn_{1-x}In_x$ NCs

Figure S10. XANES and EXAFS spectrum of $Zn_{1-x}In_x$ NCs.

Figure S11. XPS survey and fine-scanned spectrum of $Zn_{1-x}In_x$ NCs.

Figure S12. Gibbs free energy diagrams for CO_2 to $HCOOH$ on various Zn and In surfaces and their optimized configurations of reaction intermediates.

IV. References

I. Experimental Section

Synthesis of $Zn_{1-x}In_xO$ nanocrystals (NCs). Zinc chloride ($ZnCl_2$, molecular weight (MW) = $136.30 \text{ g mol}^{-1}$, 99.999% trace metal basis) and indium (III) chloride hydrate ($InCl_3 \cdot xH_2O$, MW = $221.18 \text{ g mol}^{-1}$ on anhydrous basis, 99.99%) were purchased from Sigma-Aldrich. They were mixed in a round-bottomed flask with ethanol (20 mL). Their mole ratio was varied from 0-1, using the total 2.8 mmol. The flask was fitted with a condenser and rapidly heated to $70 \text{ }^\circ\text{C}$. 5 mL aqueous ammonia solution (5%) was added dropwise under magnetic stirring after the temperature increased, and the solution becomes colloidal. The reaction was continued for 1 h and cooled to room temperature. The white precipitate was washed several times with water and ethanol until pH 7. After collecting of the precipitate and drying in air, the calcination was performed under O_2 (20 sccm)/Ar (100 sccm) flow at $400 \text{ }^\circ\text{C}$ for 2 h, producing the bright yellow oxide nanoparticles. For the characterization of samples after the CRR test, we deposited the catalysts onto the hydrophilic/water proof carbon cloth (WIZMAC Co., thickness = 0.35 mm, through-plane resistance = $1 \text{ m}\Omega$). We always stored the samples under vacuum before analysis, in order to reduce the exposure to air.

Characterization. The samples were characterized by field-emission transmission electron microscopy (FE TEM, FEI TECNAI G2 200 kV, Jeol JEM 2100F, HVEM). Energy-dispersive X-ray fluorescence spectroscopy (EDX or EDS) with elemental maps was measured using a TEM (FEI Talos F200X) operated at 200 kV that equipped with high-brightness Schottky field emission electron source (X-FEG) and Super-X EDS detector system (Bruker Super-X). This EDX has powerful sensitivity and resolution in the low photon energy region. Fast Fourier-transform (FFT) images were generated by the inversion of the TEM images using Digital Micrograph GMS1.4 software (Gatan Inc.).

High-resolution X-ray diffraction (XRD) patterns were obtained using the 9B and 3D beamlines of the Pohang Light Source (PLS) with monochromatic radiation ($\lambda = 1.5228 \text{ \AA}$). XRD pattern measurements were also carried out in a Rigaku D/MAX-2500 V/PC using Cu K_{α} radiation ($\lambda = 1.54056 \text{ \AA}$). X-ray photoelectron spectroscopy (XPS) measurements were performed using the 8A1 beam line of the PLS. X-ray absorption near edge spectra (XANES) and extended X-ray absorption fine structure (EXAFS) spectra were collected in transmission mode using the 10C beam line of the PLS with a ring current of 350 mA at 3.0 GeV. Energy calibration was carried out by simultaneously measuring the reference spectrum of metal foil. Least-squares fits of EXAFS data were performed using the Athena and Artemis software packages, version 0.9.25.

Electrochemical Measurements. The electrochemical reduction of CO₂ was conducted in a gas-tight two-compartment electrochemical cell separated by a piece of Nafion 117 membrane which was used to avoid formic acid oxidation. The NCs were tested as cathodes. 4 mg Zn_{1-x}In_xO NC sample was dispersed in Nafion (20 μ L) and isopropyl alcohol (0.98 mL). The catalyst materials (1.0 mg cm⁻²) were deposited on a glassy carbon (GC) electrode (L type, area = 0.1963 cm², Pine Instrument). The counter electrode (anode) was a Pt coil. The electrode potential was measured using an Ag/AgCl reference electrode (saturated with 4 M KCl, Pine Co.). The applied potentials (E) reported in our work were referenced to the reversible hydrogen electrode (RHE) through standard calibration. In 0.5 M KHCO₃ electrolyte (pH 7.2), $E \text{ (vs. RHE)} = E \text{ (vs. SCE)} + E_{\text{Ag/AgCl}} (= 0.197 \text{ V}) + 0.0592 \text{ pH} = E \text{ (vs. Ag/AgCl)} + 0.426 \text{ V}$. The catholyte and anolyte volumes were each minimized to 15 mL. CO₂ was continuously supplied to the cell through a gas bubbling tube during the constant potential electrolysis using an electrochemical analyzer (CompactStat, Ivium Technologies).

The gas samples were analyzed by thermal conductivity detector (TCD) and flame ionization detector (FID) equipped with a Molsieve 13X column and Porapak N column via gas chromatography (YL6500 GC). Liquid-phase products were analyzed by high performance liquid chromatography (HPLC) using a YL9100 HPLC equipped with Aminex HPX-87H column and a UV/Visible detector.

Electrochemical impedance spectroscopy (EIS) measurements were carried out for the electrode in an electrolyte by applying an AC voltage of 10 mV in the frequency range of 100 kHz to 0.1 Hz at bias voltages of -0.6 V and -0.9 V (vs. RHE). To measure double-layer capacitance via cyclic voltammetry (CV), a potential range in which no apparent Faradaic processes occur was determined from static CV. This range is -0.5 ~ -0.4 V. All measured current in this non-Faradaic potential region is assumed to be due to double-layer capacitance. The charging current, i_c , is then measured from CVs at multiple scan rates. The working electrode was held at each potential vertex for 10 s before beginning the next sweep. The charging current density (i_c) is equal to the product of the scan rate (v) and the electrochemical double-layer capacitance (C_{dl}), as given by equation $i_c = v C_{dl}$. The difference (ΔJ) between the anodic charging and cathodic discharging currents measured at -0.45 V (vs. RHE) was used for i_c . Thus, a plot of ΔJ as a function of v yields a straight line with a slope equal to $2 \times C_{dl}$. The scan rates were 20–100 mV s⁻¹.

Calculation of Electrochemical Surface Area (ECSA). The ECSA roughness factor is basically the surface area ratio between the catalyst (working electrode) vs. the metal electrode. The C_{dl} value of smooth metal electrodes is assumed to be 0.020 mF cm⁻².^{S1} Therefore, the roughness factor was evaluated by the ratio of C_{dl} for the working electrode (measured by cyclic voltammetry) and the corresponding smooth metal surface. The ECSA-corrected

HCOOH partial current density at -1.2V are calculated by the ratio of current density and roughness factor, as shown below.

Catalyst	Double layer capacitance (mF cm ⁻²)	Roughness factor	J _{HCOOH} (mA cm ⁻²)	ECSA-normalized J _{HCOOH} (mA cm ⁻²)
Zn	5.8	290	1.875	0.006
Zn _{0.95} In _{0.05}	3.7	185	21.575	0.117
Zn _{0.7} In _{0.3}	2.6	130	14.223	0.109
Zn _{0.3} In _{0.7}	2.2	110	10.402	0.095
In	2	100	6.881	0.069

Calculation. First-principles calculations were performed via spin-polarized density functional theory (DFT), as implemented in the Vienna *ab initio* simulation package (VASP).^{S2,S3} The projected augmented plane wave (PAW)^{S4,S5} approach with a plane-wave kinetic energy cutoff of 400 eV, and the Perdew-Burke-Ernzerhof (PBE)^{S6} exchange-correlation functional were employed. The effect of attractive van der Waals (vdW) interaction was taken into account by employing Grimme's D3 correction (PBE-D3).^{S7} The Methfessel-Paxton method with a broadening of 0.1 eV is used for slabs, while the Gaussian-smearing with 0.01 eV was used for molecules. Total energy of a system was taken by extrapolating the smearing parameter to zero K.

A vacuum space of 15 Å was used along the Z-direction (perpendicular to the slabs) to ensure that no appreciable interaction occurred between adjacent images. Structural optimization was performed until the average force was < 0.03 eV/Å and the total energy converged within 10⁻⁵ eV/atom. A Monkhorst-Pack *k*-point sampling of 3 × 3 × 1 was used for slab geometry, while only Γ-point was used for molecules.

Indium (101), (110), and (112) surfaces were represented by three layers of (3×3) periodic supercells.^{S8} The (101) facet represents a dominant crystal plane as identified from the XRD experiment (see Fig. S6 below). Although less stable, other three phases were chosen to investigate the effect of different facets on the reaction. Zinc (002) and (101) surfaces were modelled by (4×4) and (2×4) supercells, respectively. The (101) facet was also known to be the preferential facet of the hexagonal Zn identified from our XRD peaks (see Fig. S6 below). The Zn (002) facet was considered for the same reason as other less stable In surfaces. The Zn_{0.95}In_{0.05} bimetallic catalytic surface was built by adsorbing four In atoms on the three-layer (5×5) Zn (002) surface, where the In atoms were taken from (2×2) monolayer. It is worth mentioning that a similar model was used for copper-Indium bimetallic catalyst.^{S9} The reason for using Zn (002) surface in the alloy will be clear in the main text. In all cases, the bottom-most layer was fixed during optimization, while all other atoms were allowed to relax freely.

At 298 K and 1 atm, the Gibbs free energy was calculated according to:

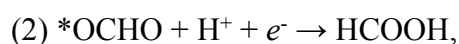
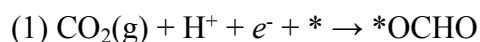
$$G = E_{DFT} + E_{ZPE} + \int_0^{298} C_V dT - TS,$$

where E_{DFT} is the total energy obtained from the DFT calculation, E_{ZPE} is the zero point energy

correction, and $\int_0^{298} C_V dT$ is the reaction enthalpy change from 0 to 298 K, and TS is the entropy correction. Gas phase molecules, CO₂ and H₂, were treated as ideal gas, while adsorbates were treated using the harmonic approximation. For the frequency calculation of gas molecules, the PBE/6-311++G** level was employed using Gaussian09.^{S10} Following **Table S0** gives each contribution to the free energy of the gas molecules. In addition, the DFT energy of gaseous

CO₂, HCOOH, and H₂ were corrected by 0.41 eV, 0.20 eV, and 0.09 eV, respectively, to account for inherent errors in the DFT for C=O double bonds.^{S11-S13}

The computational hydrogen electrode model (CHE)^{S14} was employed to calculate the change in Gibbs free energy, ΔG, along the reaction path. The conversion from CO₂ to HCOOH was calculated based on the following elementary reactions:^{S15-S17}



Where an asterisk (*) designates that the intermediate (*OCHO) was adsorbed on the catalytic surface. On each surface, the most stable adsorption geometry of the intermediate was considered for the further calculation among 3~6 different ones.

Table S0. Zero-point energy correction (E_{ZPE}), enthalpy correction ($\int_0^{298} C_V dT$), and entropy correction (TS) for gaseous molecules at the partial pressure of 1 atm for CO₂ and H₂, and of 2 Pa for HCOOH. Gas phase corrections were applied to CO₂ and HCOOH with the value of 0.13 and -0.08 eV, respectively.^{S18} All values are given in eV.

Species	E_{ZPE}	$\int_0^{298} C_V dT$	TS
CO ₂	0.31	0.10	0.66
H ₂	0.27	0.06	0.40
HCOOH	0.89	0.11	1.05

Table S1. Comparison of CRR catalytic activity on In-based catalysts in the literatures; total current density (J) and faradic efficiency (FE) for HCOOH (FE_{HCOOH}) at a potential (vs. RHE), and production rate of HCOOH.

No.	Materials (electrolyte)	Potential (V) vs. RHE	J (mA cm ⁻²) (scan rate)	FE (%)	Rate (mmol h ⁻¹ cm ⁻²)
S19	Anodized In (0.1 M K ₂ SO ₄ , pH 4.4)	-1.2	~ -1 (50 mV s ⁻¹)	70	--
S20	In/Carbon (0.1 M K ₂ SO ₄ , pH 4.4)	-1.45	-6.1	45	--
S21	In _{0.9} Sn _{0.1} alloy (0.1 M of KHCO ₃)	-1.2	-43.8 (50 mV s ⁻¹)	96.5	--
S22	MoP@In/Carbon (30 wt% [Bmim]PF ₆ /MeCN/H ₂ O)	-2.0	-30	98	--
S23	In (III) protoporphyrin @carbon (0.1 M phosphate buffer, pH 9.6)	-1.5	-30	75	--
S24	In ₂ O ₃ @carbon (0.5 M KHCO ₃)	-1.0	-18 (50 mV s ⁻¹)	87.6	--
S25	In dendrite foams on Cu substrates (0.5 M KHCO ₃ , pH 7.2)	-0.86	-5.8 (25 mV s ⁻¹)	86	--
S26	In on graphite (0.05 M KHCO ₃ , pH 6.5)	-2.0	-35	94.5	0.136
S8	3D hierarchical porous In on Cu mesh (0.1 M KHCO ₃)	-1.2	-70 (50 mV s ⁻¹)	90	1.14
S27	Sulfur-doped In on C fibers (0.5 M KHCO ₃ , pH 7.2)	-1.23	-80	93	1.449
S28	In ₂ O ₃ @reduced graphene oxide	-1.2	-23	84.6	--
Present work	Zn _{0.95} In _{0.05} bimetal (0.5 M KHCO ₃ , pH 7.2)	-1.2	-22 (5 mV s ⁻¹)	95	0.40

II. Supporting Figures

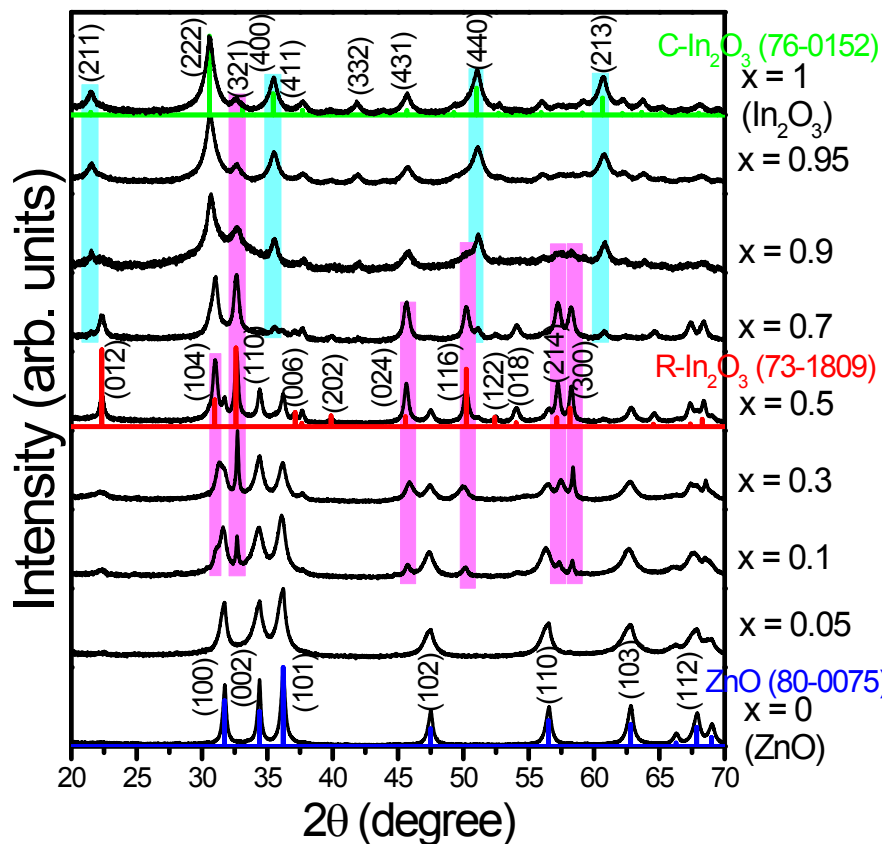


Figure S1. XRD patterns of Zn_{1-x}In_xO NCs with $x = 0, 0.05, 0.1, 0.3, 0.5, 0.7, 0.9, 0.95,$ and 1 . The peaks were referenced to those of the hexagonal wurtzite (WZ) phase ZnO (JCPDS No. 80-0075, $a = 3.253 \text{ \AA}$ and $c = 5.209 \text{ \AA}$), rhombohedral (R) phase In₂O₃ (JCPDS No. 73-1809, $a = 5.490 \text{ \AA}$ and $c = 14.520 \text{ \AA}$), and cubic (C) phase In₂O₃ (JCPDS No. 76-0152, $a = 10.12 \text{ \AA}$).

At $x = 0$, the NC sample consisted of WZ phase ZnO phase, whose XRD peaks are matched to hexagonal wurtzite (WZ) phase ZnO (JCPDS No. 80-0075, $a = 3.253 \text{ \AA}$ and $c = 5.209 \text{ \AA}$). The sample of $x = 0.05$ shows only WZ phase ZnO peaks, indicating that the 5% In doped into the ZnO NCs. As x increases, the R phase In₂O₃ (JCPDS No. 73-1809, $a = 5.490 \text{ \AA}$ and $c = 14.520 \text{ \AA}$) peaks appear as marked by pink bars, indicating that R phase In₂O₃ and WZ phase ZnO NCs coexist. The C phase In₂O₃ peaks (JCPDS No. 76-0152, $a = 10.12 \text{ \AA}$), marked by sky blue bars, appear for $x = 0.7-1$, and the intensity becomes larger with increasing x . At $x = 1$ (In₂O₃), the major phase is C phase, but the R phase exists as an impurity phase.

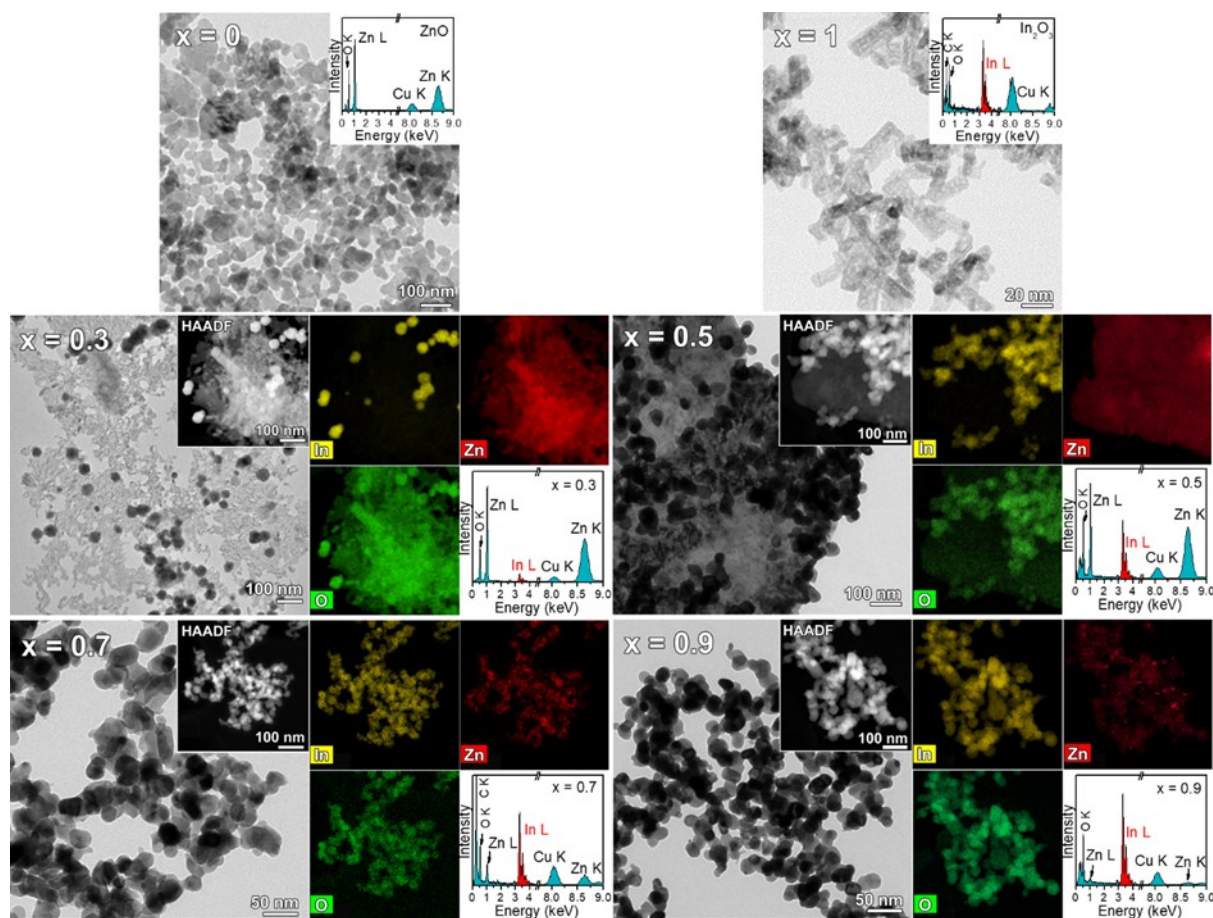


Figure S2. High-resolution TEM (HRTEM) images, high-angle annular dark-field scanning TEM (HAADF-STEM) images, EDX elemental mapping, and EDX spectrum of $\text{Zn}_{1-x}\text{In}_x\text{O}$ with $x = 0, 0.3, 0.5, 0.7, 0.9,$ and 1 . They are consisted of ZnO and In_2O_3 nanocrystals.

At $x = 0$ (ZnO), the WZ phase ZnO nanocrystals (NCs) exhibit a spherical morphology with an average size of 50 nm . At $x = 0.3$ and 0.5 , the ZnO NCs form a network structure and the R phase In_2O_3 NCs embedded into the ZnO NCs. The average size of In_2O_3 NCs is 50 nm . As x increases to 0.7 and 0.9 , the C phase In_2O_3 NCs becomes dominant and the size decreases to 30 nm . At $x = 1$, the C phase In_2O_3 exhibit a rectangular shape with an average size of about 20 nm . The EDX spectrum shows the In/Zn ratio for each sample.

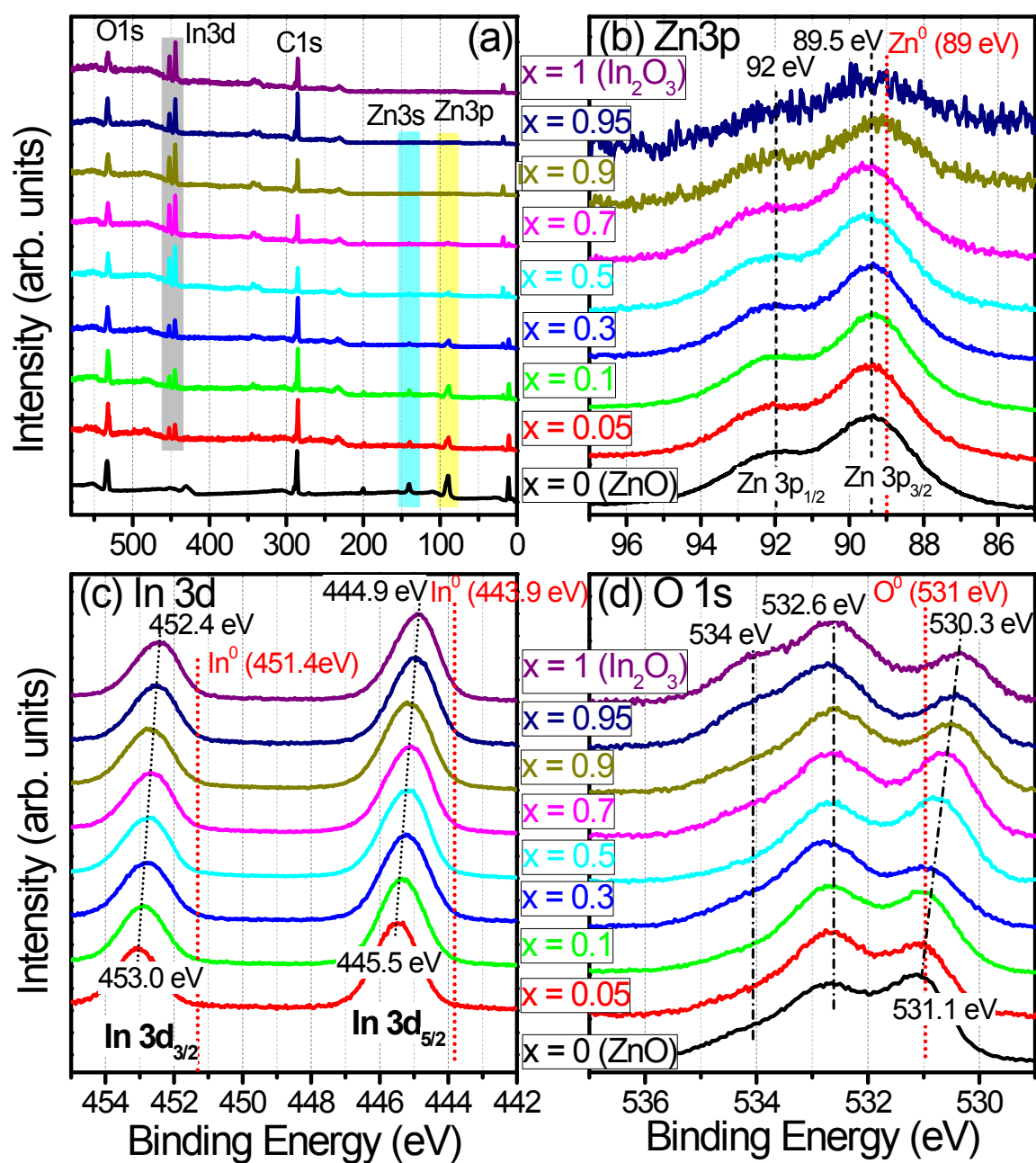


Figure S3. (a) XPS survey scans of Zn_{1-x}In_xO with $x = 0, 0.05, 0.1, 0.3, 0.5, 0.7, 0.9, 0.95,$ and 1. Fine-scan (b) Zn 3p, (c) In 3d, and (d) O 1s peak.

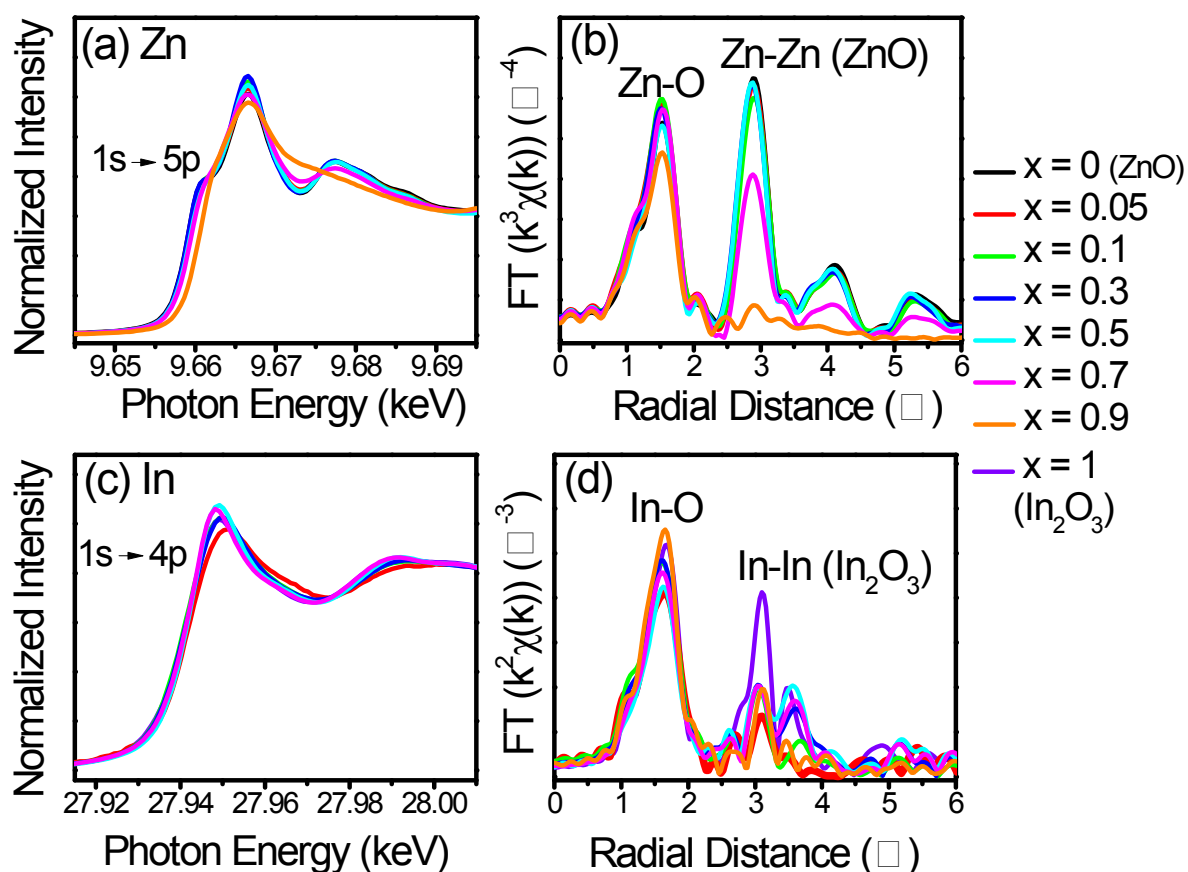
(a) XPS survey scans shows that as x increases, the intensity of Zn peaks decreases while the intensity of In peaks increase. The relative ratio of Zn 3p and In 3d peak provides the composition of samples, consistent with the value of EDX data.

(b) The Zn 3p_{3/2} and Zn 3p_{1/2} peaks are separated by about 2.5 eV. The samples show the Zn

$3p_{3/2}$ peak of Zn-O bonding structures at 89.5 eV, which is 0.5 eV blue-shifted with respect to that of neutral Zn (Zn^0) at 89 eV.

(c) The In $3d_{5/2}$ and In $3d_{3/2}$ peaks are separated by 7.54 eV. At $x = 0$, the In_2O_3 NCs show the peaks at 444.9 and 452.4 eV, which are 1.0 eV blue-shifted with respect to those of neutral In (In^0) at 443.9 and 451.4 eV, respectively. As Zn content increases, the peaks are blue shifted continuously. For $x = 0.05$, the peaks appear at 445.5 and 453.0 eV, corresponding to 1.6 eV blue shift. As shown in the analysis of O 1s, the ZnO-rich phase (lower x) has more oxygen vacancies. Therefore, the higher binding energy can be explained by a model that the In cations bind with OH anions at the oxygen vacancies and thus experience the electron depletion.

(d) The In_2O_3 shows three O 1s peaks: 530.3 eV for the lattice oxygen (O^{2-}), 532.6 eV for adsorbed O_2 or OH^- ions, and 534 eV for adsorbed H_2O . The binding energy of neutral O (O^0) is 531 eV. As the Zn content increases, the lattice oxygen peak shifts to 531.1 eV, which is ascribed to the O_2^{2-}/O^- defect species at the enriched oxygen vacancy sites.^{S29-S34}



F

Figure S4. (a) XANES and (b) EXAFS spectra above the Zn K edge and (c) XANES and (d) EXAFS spectra above the In K edge for $\text{Zn}_{1-x}\text{In}_x\text{O}$ with $x = 0, 0.05, 0.1, 0.3, 0.5, 0.7, 0.9,$ and 1.

The evolution of the local crystal structure of Zn and In upon the change of composition was probed with their K-edge X-ray absorption near edge spectra (XANES) and extended X-ray absorption fine structure (EXAFS).

(a) XANES spectra above the Zn K edge consisted of $1s \rightarrow 4p$ transition. The peak feature is nearly the same for $x = 0-0.5$, but it becomes flattened with increasing $x (= 0.7-0.9)$. This feature change can be explained by a model that the Zn is dominantly doped into the In_2O_3 NCs at the higher x .

(b) Non-phase-corrected k^3 -weighted Fourier-transformed extended X-ray absorption fine structure (FT EXAFS) consisted of two peaks, corresponding to Zn-O ($d_{\text{Zn-O}} = 1.8-1.86 \text{ \AA}$) and Zn-Zn bonds ($d_{\text{Zn-Zn}} = 3.16-3.19 \text{ \AA}$) of ZnO. The $x = 0.9$ sample shows no Zn-Zn peaks,

probably due to the doping of all Zn into In_2O_3 , consistently with the XANES data. As x increases, the relative intensity of Zn-O vs. Zn-Zn peaks increases, indicating the more oxide layers.

(c) XANES spectra above the In K edge consisted of $1s \rightarrow 5p$ transition. The peak feature is nearly the same for $x = 0.5-1$, but becomes flattened and its peak intensity decreases with decreasing x . This change is ascribed to the In doping into ZnO NCs.

(d) Non-phase-corrected k^2 -weighted FT EXAFS consisted of two peaks, corresponding to In-O ($d_{\text{In-O}} = 1.93-2.00 \text{ \AA}$) and In-In bonds ($d_{\text{In-In}} = 3.40-3.42 \text{ \AA}$) of In_2O_3 . In the binary phase, the relative intensity of In-O vs. In-In peaks show a tendency of increase with x . The more oxide layers at the higher x is consistent with the EXAFS data of Zn K edge peak.

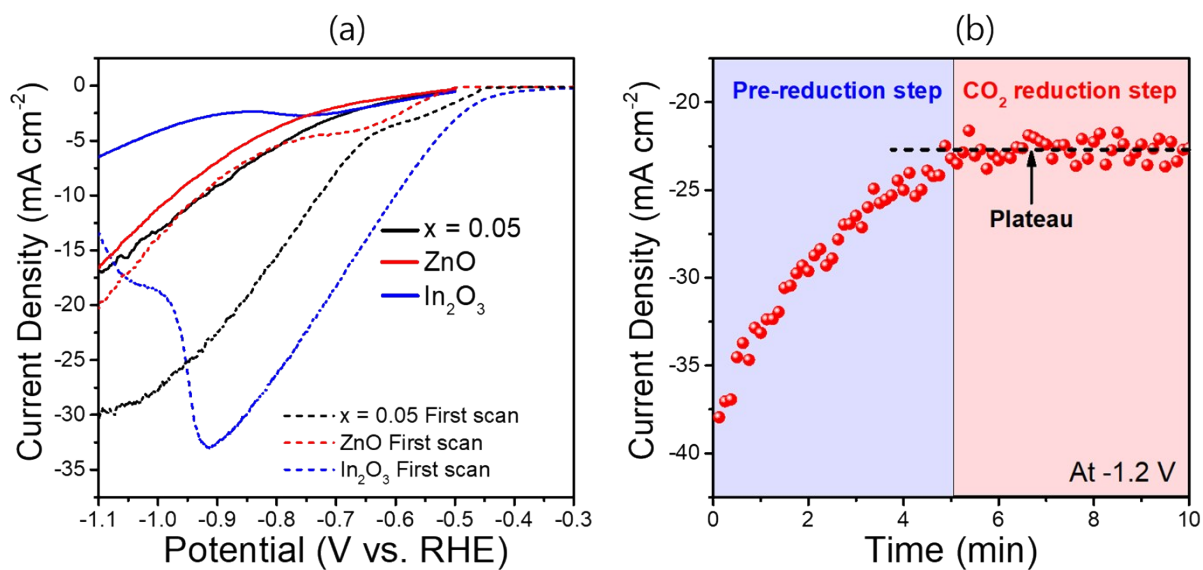


Figure S5. (a) LSV curves of catalysts for the first scan (in CO_2 -saturated 0.5 M KHCO_3 electrolyte (pH 7.2) and (b) current density vs. time to show the pre-reduction step for $x = 0.05$ sample.

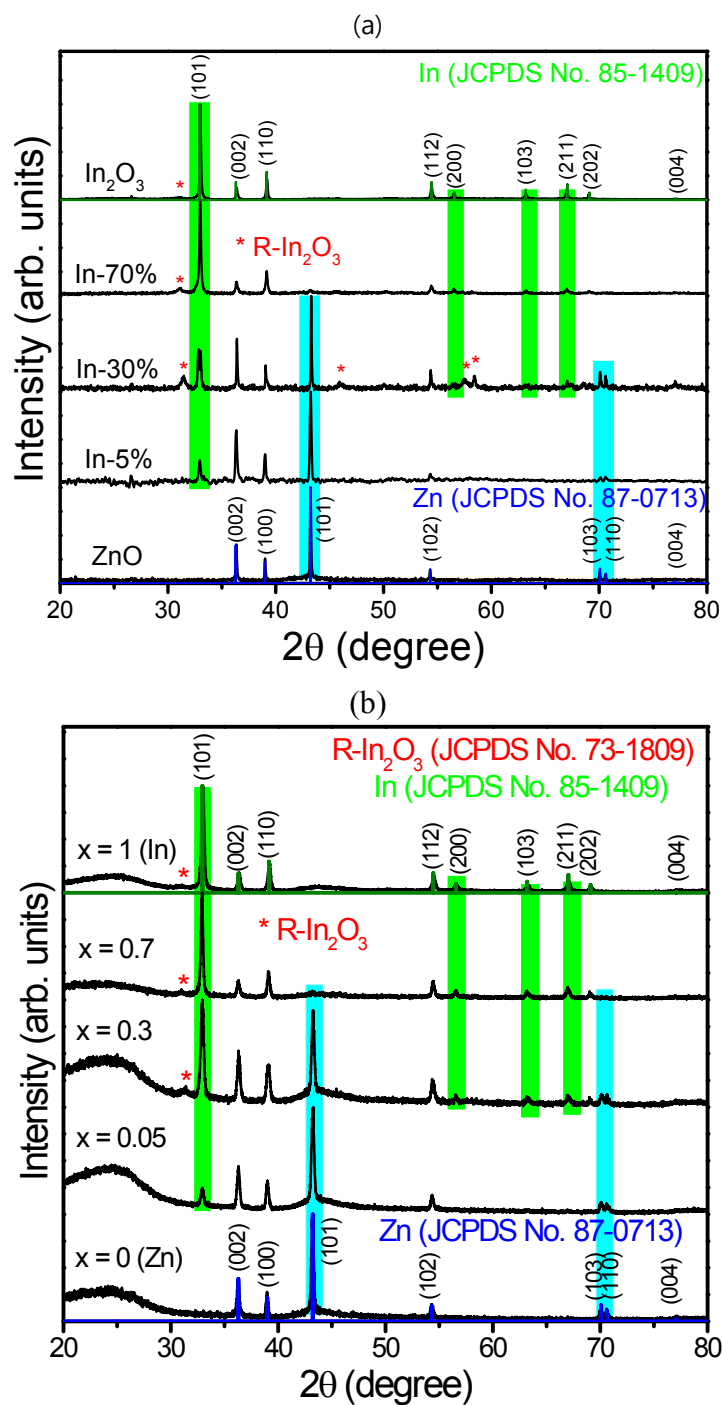
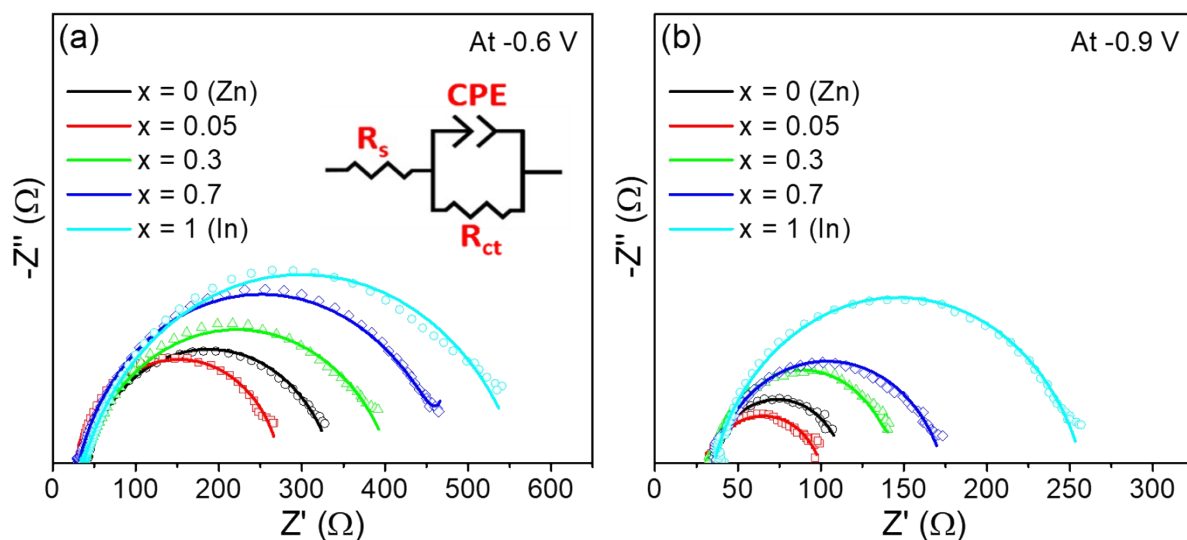


Figure S6. XRD patterns of $\text{Zn}_{1-x}\text{In}_x$ ($x = 0, 0.05, 0.3, 0.7,$ and 1) samples, measured (a) after 10 min pre-reduction and (b) 2 h CRR at -1.2 V (vs. RHE). The peaks were referenced to those of the hexagonal phase Zn (JCPDS No. 87-0713, $a = 2.665$ Å and $c = 4.947$ Å), tetragonal phase In (JCPDS No. 85-1409, $a = 3.251$ Å and $c = 4.945$ Å), and rhombohedral (R) phase In_2O_3 (JCPDS No. 73-1809, $a = 5.490$ Å and $c = 14.520$ Å).

ZnO is transformed into the hexagonal phase Zn metal (JCPDS No. 87-0713, $a = 2.665 \text{ \AA}$ and $c = 4.947 \text{ \AA}$) upon electrochemical CRR process. At $x = 0.05$, both Zn and In metals are produced, where the latter one is produced by the reduction of the doped In ions (in ZnO NCs). The In peaks (marked by green box) are matched to those of tetragonal phase In (JCPDS No. 85-1409, $a = 3.251 \text{ \AA}$ and $c = 4.945 \text{ \AA}$). Many peaks of Zn and In is overlapped; e.g., (002) Zn and (002) In, (100) Zn and (110) In, (102) Zn and (112) In. The $x = 0.05, 0.3$ and 0.7 samples show both Zn (marked by sky-blue box)) and In peaks, indicating that the ZnO and In_2O_3 are reduced to Zn and In metals, respectively. For $x = 0.3-1$, the peaks of R phase In_2O_3 remain as impurity level, while those of C phase In_2O_3 disappeared. It indicates that the reduction efficiency of R phase In_2O_3 is lower than that of C phase In_2O_3 .



Sample	R_s (Ω)	R_{ct} (Ω)
x = 0 (Zn)	30.6	298
x = 0.05	30.5	243
x = 0.3	35.9	372
x = 0.7	32.2	469
x = 1 (In)	37.6	563

Sample	R_s (Ω)	R_{ct} (Ω)
x = 0 (Zn)	34.2	79.8
x = 0.05	32.2	68.2
x = 0.3	34.5	105
x = 0.7	35.5	139
x = 1 (In)	36.7	221

Figure S7. Nyquist plots for EIS measurements of $Zn_{1-x}In_x$ NCs with $x = 0, 0.05, 0.3, 0.7$ and 1 , using the frequency in the range from 100 kHz to 0.1 Hz at a representative potential of (a) -0.6 V and (b) -0.9 V (vs. RHE) in CO_2 -saturated 0.5 M $KHCO_3$ electrolyte (pH 7.2). The modified Randles circuit for fitting is shown in the inset.

Electrochemical impedance spectroscopy (EIS) measurements of the samples were performed using a 100 kHz– 0.1 Hz frequency range and an amplitude of 10 mV at -0.6 V and -0.9 V (vs. RHE). In the high-frequency limit and under non-Faradaic conditions, the electrochemical system is approximated by the modified Randles circuit shown in the inset, where R_s denotes the solution resistance, CPE is a constant-phase element related to the double-layer capacitance, and R_{ct} is the charge-transfer resistance from any residual Faradaic processes. A semicircle in the low-frequency region of the Nyquist plots represents the charge transfer process, with the diameter of the semicircle reflecting the charge-transfer resistance. The real (Z') and negative imaginary ($-Z''$) components of the impedance are plotted on the x and y axes, respectively. The simulation of the EIS spectra using an equivalent circuit model allowed us to determine the charge transfer resistance, R_{ct} , which is a key parameter for characterizing the catalyst-electrolyte charge transfer process. The fitting parameters are listed in the table

below the figure. The R_{ct} values follow an order consistent with the CRR performance.

At -0.6 V, where there are almost no electrochemical reactions, $x = 0.05$ electrodes exhibit smallest R_{ct} value among the samples, indicating that it has the lowest charge-transfer resistance. The R_{ct} value decreased with increasing x . As the CRR reaction occurs at -0.9 V, the kinetics of electron-transfer processes on the electrodes reduced the R_{ct} value. The EIS responses are consistent well with the CRR performance.

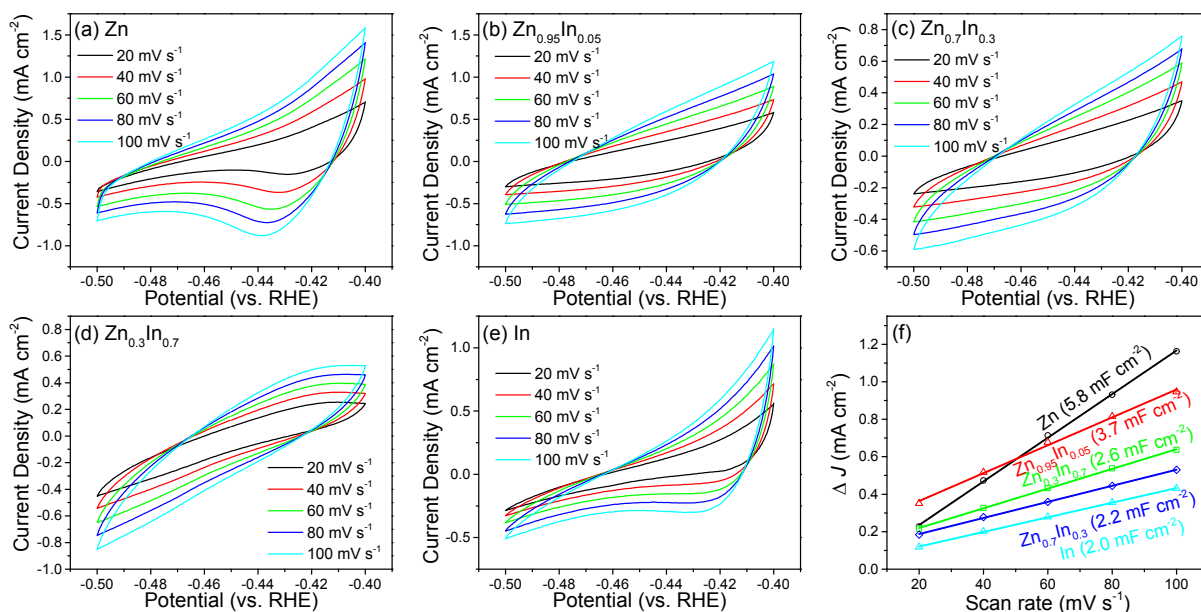


Figure S8. Cyclic voltammograms of $\text{Zn}_{1-x}\text{In}_x$ NCs with (a) $x = 0$, (b) $x = 0.05$, (c) $x = 0.3$, (d) 0.7 and (e) 1 , in a non-Faradaic region ($-0.5 \sim -0.4$ V vs. RHE), at 20 - 100 mV s^{-1} scan rates (with a step of 20 mV s^{-1}) in CO_2 -saturated 0.5 M KHCO_3 electrolyte ($\text{pH } 7.2$). (e) Difference (ΔJ) between the anodic charging and cathodic discharging currents measured at -0.45 V (vs. RHE) and plotted as a function of the scan rate. The value in parenthesis represents the C_{dl} , obtained by the half of the linear slope.

Cyclic voltammograms were measured at $-0.5 \sim -0.4$ V, in a non-Faradaic region, using various scan rates. The double-layer capacitance (C_{dl}) was obtained as the slope (half value) of a linear fit of ΔJ vs. scan rate (20 - 100 mV s^{-1}), where ΔJ is the difference between the anodic charging (positive value) and cathodic discharging currents (positive value). The C_{dl} value is 5.8 , 3.7 , 2.6 , and 2.0 mF cm^{-2} for $x = 0$, 0.05 , 0.3 , 0.7 and 1 , respectively. The C_{dl} value decreases with increasing x , consistently with the concentration dependence of CRR performance. Therefore, the double-layer capacitance determines the CRR catalytic activity of $\text{Zn}_{1-x}\text{In}_x$ samples.

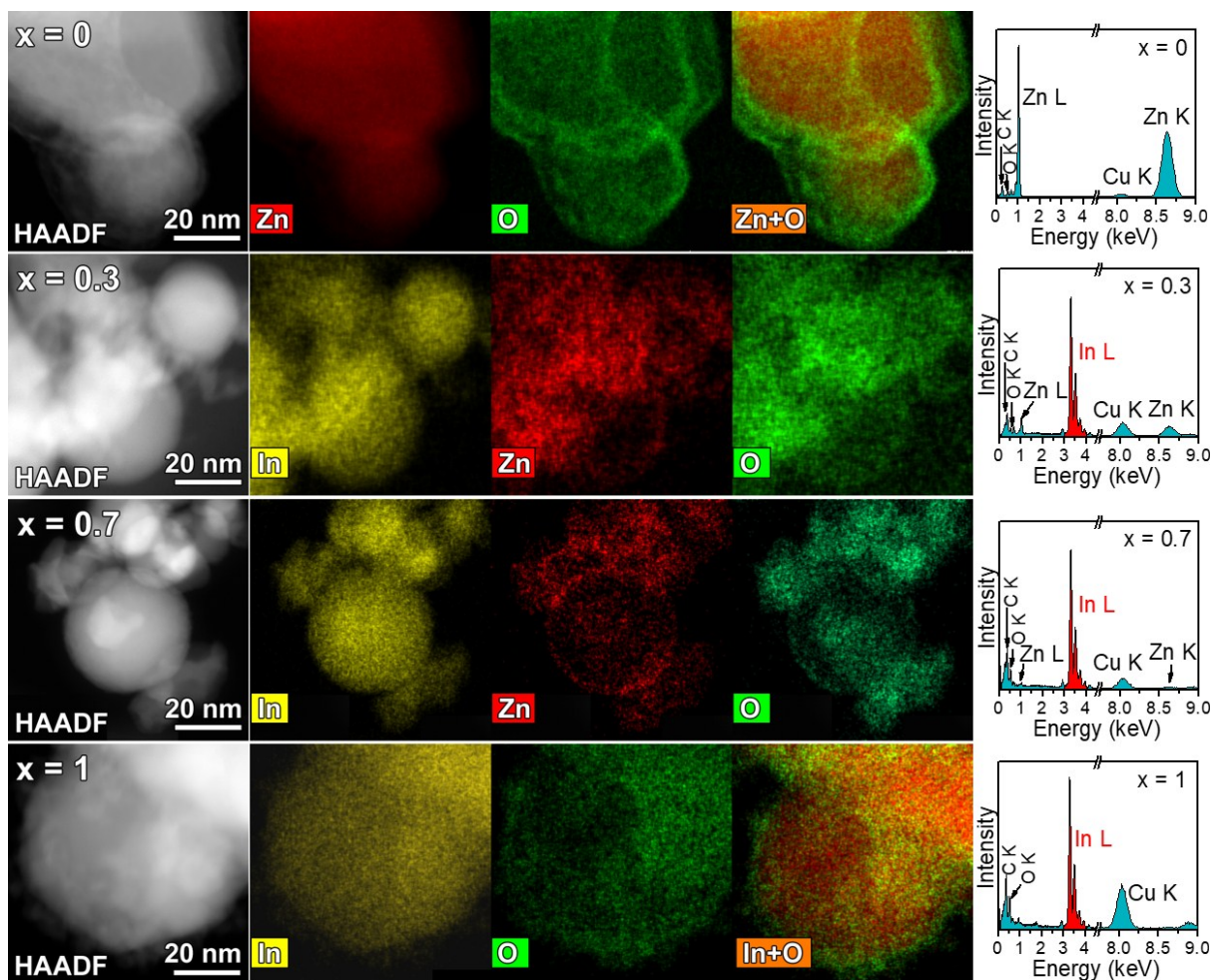


Figure S9. HAADF-STEM images, EDX elemental mapping, and EDX spectrum of $\text{Zn}_{1-x}\text{In}_x$ with $x = 0, 0.3, 0.7,$ and 1 . They are consisted of Zn and In NCs.

At $x = 0$, the Zn NCs are sheathed with the oxide layer shell. At $x = 0.3$, the In NCs (size = 10–30 nm) exhibits a spherical morphology, while the Zn NCs have no particular shape. At $x = 0.7$, the spherical shaped In NCs are surrounded by the Zn NCs. As x increases, the oxide layers exist over whole NCs. At $x = 1$, the average size of In NCs is 50 nm. The EDX spectrum shows that the ratio of In/Zn ratio increases with x .

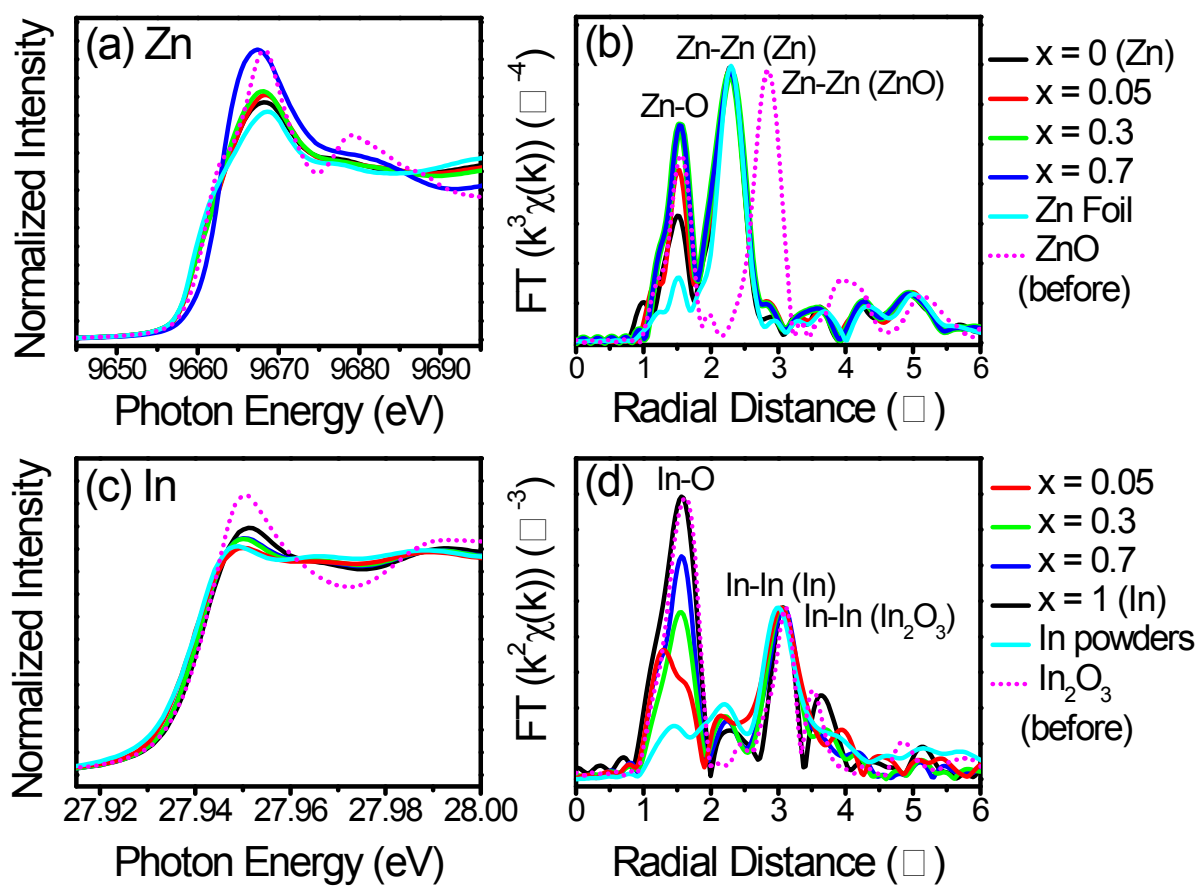


Figure S10. (a) XANES and (b) EXAFS spectra above the Zn K edge and (c) XANES and (d) EXAFS spectra above the In K edge for the $\text{Zn}_{1-x}\text{In}_x$ bimetallic catalysts after 2h electrochemical CRR of $\text{Zn}_{1-x}\text{In}_x\text{O}$ NCs with $x = 0, 0.05, 0.3, 0.7,$ and 1 , and the reference samples such as ZnO NCs (before reduction), In_2O_3 NCs (before reduction), Zn foil, and In powder.

(a) XANES spectra above the Zn K edge, consisted of $1s \rightarrow 4p$ transition. After the CRR, the peak feature of Zn-In bimetallic catalysts becomes closer to that of Zn foil. The $x = 0.7$ exhibits the larger intensity than the others, probably due to the dominant oxide form.

(b) Non-phase-corrected k^3 -weighted FT EXAFS of catalyst samples consisted of two peaks, corresponding to Zn-O ($d_{\text{Zn-O}} = 1.80\text{-}1.86 \text{ \AA}$) and Zn-Zn bond ($d_{\text{Zn-Zn}} = 2.50\text{-}2.52 \text{ \AA}$). The Zn-Zn bond distance is matched with that of Zn foil. The appearance of Zn-O peak indicates the amorphous oxide layers sheathing the Zn NCs. The relative intensity of Zn-O/Zn-Zn peak increases with increasing x , suggesting that the oxide layers becomes significant.

(c) XANES spectra above the In K edge consisted of $1s \rightarrow 5p$ transition. The samples exhibit the peak feature that is closer to that of In powder.

(d) Non-phase-corrected k^2 -weighted FT EXAFS of consisted of two peaks, corresponding to In-O ($d_{\text{In-O}} = 1.93\text{-}2.00 \text{ \AA}$) and In-In bonds ($d_{\text{In-In}} = 3.31\text{-}3.43 \text{ \AA}$). The In-In distance is closer to that of In metal powders. All samples show the metallic In-In peaks with the In-O peaks, indicating that the In NCs are sheathed with the oxide layers. The relative intensity of In-O/In-In peak increases with increasing x , suggesting that the oxide layers becomes significant, consistent with the EXAFS data of Zn K-edge peak.

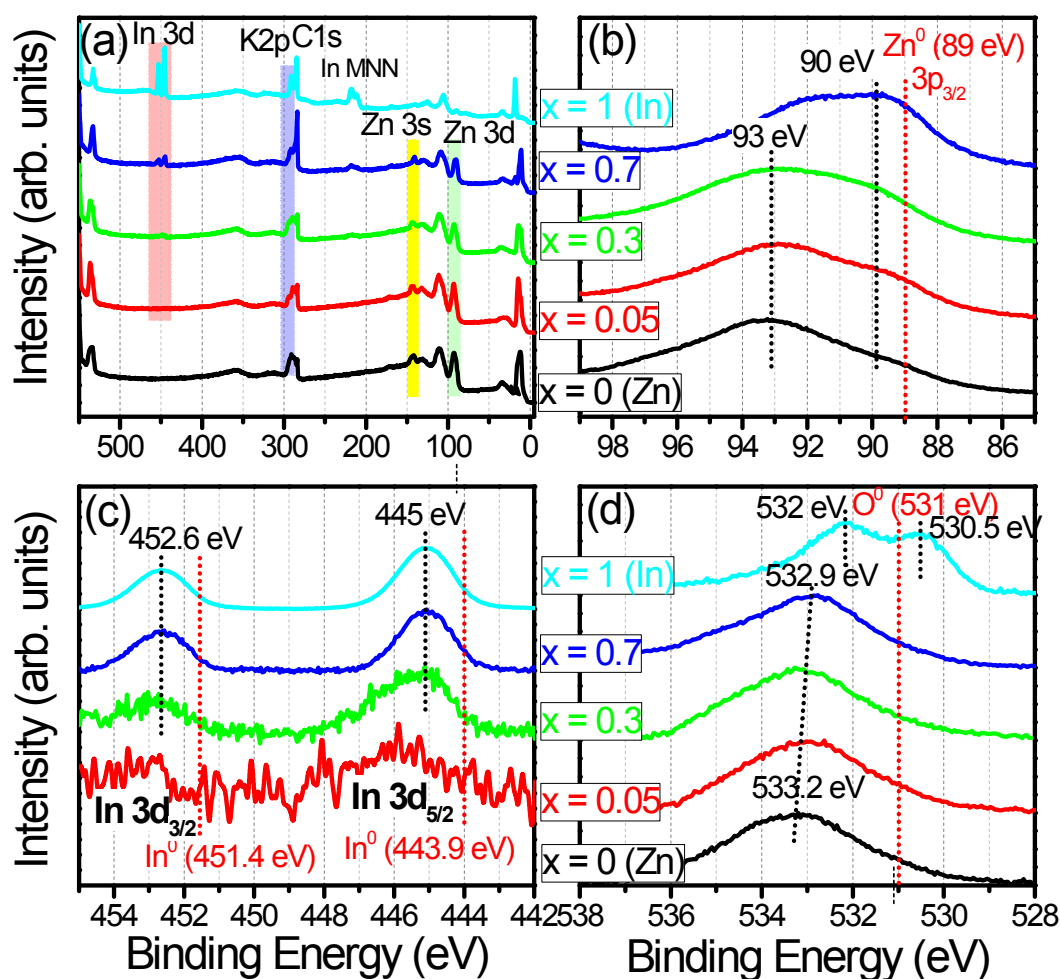


Figure S11. (a) XPS survey scans of the $Zn_{1-x}In_x$ bimetallic catalysts synthesized by the electrochemical reduction of $Zn_{1-x}In_xO$ NCs with $x = 0, 0.05, 0.3, 0.7,$ and 1 . Fine-scan (b) Zn 3p, (c) In 3d, and (d) O 1s peaks.

(a) XPS survey scans show that as x increases, the intensity of Zn peaks decreases while the intensity of In peaks increases. The K 2p peaks are originated from the electrolyte ($KHCO_3$).

(b) The Zn $3p_{3/2}$ and Zn $3p_{1/2}$ peaks, separated by about 2.5 eV, becomes broader than those of before reduction. The neutral Zn (Zn^0) $3p_{3/2}$ should appear at 89 eV. The samples show the peaks at 93 and 90 eV, which are assigned to the Zn-O peak, indicating that the oxide layers sheath the Zn NCs. As x decreases, the intensity of 93 eV peak increases. There we assigned this to the Zn bonding states that coordinated with carbonate of the electrolyte. We suggest that as x decreases, the Zn NCs are more coordinated with the electrolyte

(c) The sample shows the In $3d_{5/2}$ and In $3d_{3/2}$ peaks at 445.0 and 452.6 eV, which are 1.1 eV

blue-shifted with respect to the signal of neutral In (In^0) at 443.9 and 451.4 eV, respectively. It indicates that the electronic states correspond to those of the oxide.

(d) The In ($x = 1$) NCs shows two peaks: 530.5 eV for the lattice oxygen (O^{2-}) and 532 eV for adsorbed O_2 or OH^- ions. The former peaks would be originated from the R phase In_2O_3 residual. The binding energy of neutral O (O^0) is 531 eV. The Zn containing samples shows the broad oxygen peak at 532.9-533.2 eV, which is ascribed to the adsorption of carbonate of electrolyte.

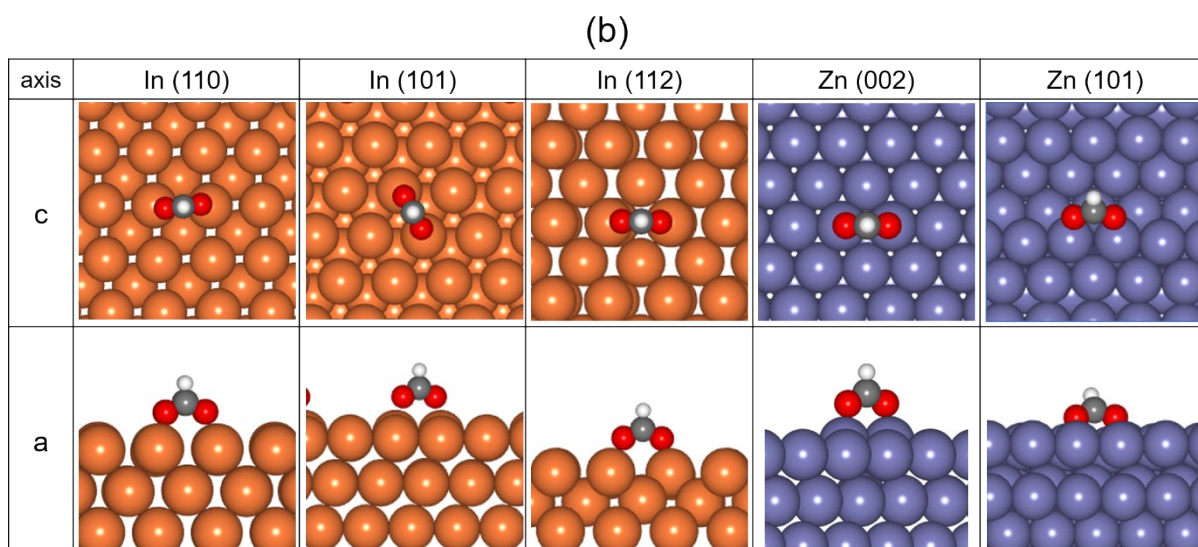
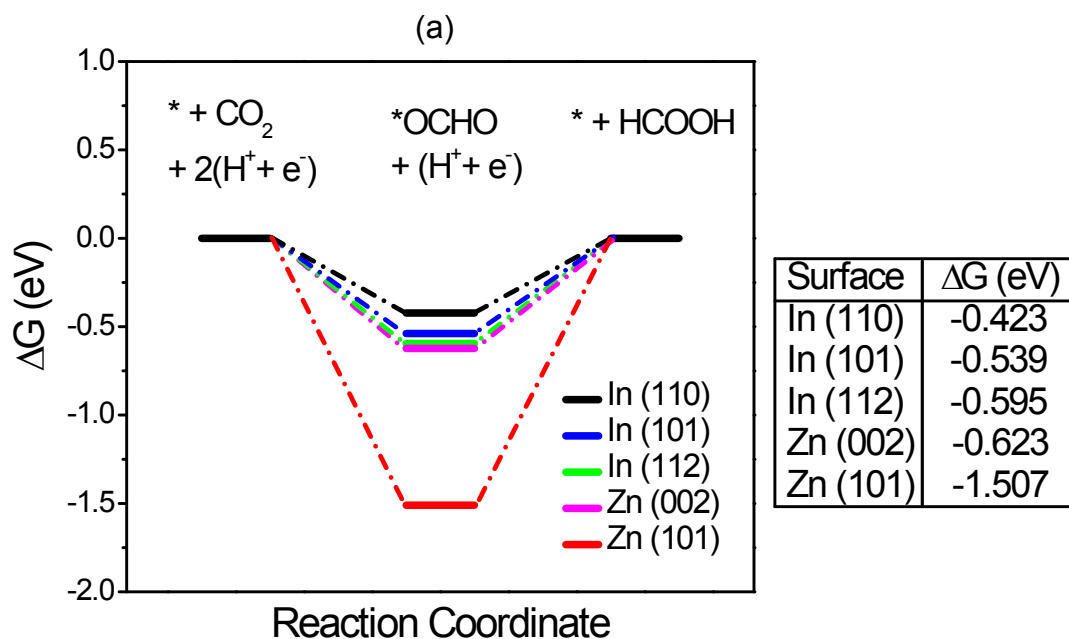


Figure S12. (a) Gibbs free energy (ΔG) diagrams for CO_2 to HCOOH on In (110), In (101), In (112), Zn (002), and Zn (101) surfaces. ΔG denotes the free energy change of the intermediate with respect to the reactants. (b) Optimized configurations of reaction intermediates ($^*\text{OCHO}$) on each surface in top (c-axis) and side (a-axis) views. Zn: bluish purple, In: brown, C: gray, O: red, and H: white.

Three different In surfaces, i.e., (101), (110), and (112) surfaces, were modelled by three layers (3×3) periodic supercells. The ΔG is -0.423, -0.539, and -0.595 eV, respectively, on In (110), In (101), and In (112), indicating that the In (110) is most energetically favorable among three facets. On the one hand, (4×4) and (2×4) unit cells were chosen for Zn (002) and Zn (101) surfaces. The ΔG is -0.623 and -1.507 eV, respectively, on Zn (002) and Zn (101), indicating that the Zn (002) facet is more energetically favorable for HCOOH compared to Zn (101). These Zn surfaces are less favorable for the HCOOH production than the In.

IV. References

- S1. W. Ma, S. Xie, X. -G. Zhang, F. Sun, J. Kang, Z. Jiang, Q. Zhang, D. -Y. Wu and Y. Wang, *Nat. Commun.*, 2019, **10**, 892.
- S2. G. Kresse and J. Furthmüller, *Phys. Rev. B*, 1996, **54**, 11169-11186.
- S3. G. Kresse and J. Furthmüller, *Comput. Mater. Sci.*, 1996, **6**, 15-50.
- S4. J. P. Perdew, K. Burke and M. Ernzerhof, *Phys. Rev. Lett.*, 1996, **77**, 3865-3868.
- S5. P. E. Blöchl, *Phys. Rev. B*, 1994, **50**, 17953-17979.
- S6. G. Kresse and D. Joubert, *Phys. Rev. B*, 1999, **59**, 1758-1775.
- S7. S. Grimme, J. Antony, S. Ehrlich and H. Krieg, *J. Chem. Phys.*, 2010, **132**, 154104.
- S8. W. Luo, W. Xie, M. Li, J. Zhang and A. Züttel, *J. Mater. Chem. A*, 2019, **7**, 4505-4515.
- S9. W. Luo, W. Xie, R. Mutschler, E. Oveisi, G. L. de Gregorio, R. Buonsanti and A. Züttel, *ACS Catal.*, 2018, **8**, 6571-6581.
- S10. K. Chang, H. Zhang, J. G. Chen, Q. Lu, M. -J. Cheng, *ACS Catal.*, 2019, **9**, 8197-8207.
- S11. J. S. Yoo, R. Christensen, T. Vegge, J. K. Nørskov and F. Studt, *ChemSusChem*, 2016, **9**, 358-363.
- S12. F. Studt, M. Behrens, E. L. Kunkes, N. Thomas, S. Zander, A. Tarasov, J. Schumann, E. Frei, J. B. Varley, F. Abild-Pedersen, J. K. Nørskov and R. Schlögl, *ChemCatChem*, 2015, **7**, 1105-1111.
- S13. R. Christensen, H. A. Hansen and T. Vegge, *Catal. Sci. & Tech.*, 2015, **5**, 4946-4949.
- S14. A. A. Peterson, F. Abild-Pedersen, F. Studt, J. Rossmeisl and J. K. Nørskov, *Energy & Environmental Science*, 2010, **3**, 1311-1315.
- S15. B. Jiang, X. -G. Zhang, K. Jiang, D. -Y. Wu and W. -B. Cai, *J. Am. Chem. Soc.*, 2018, **140**, 2880-2889.
- S16. S. Zhang, P. Kang and T. J. Meyer, *J. Am. Chem. Soc.*, 2014, **136**, 1734-1737.
- S17. A. Klinkova, P. De Luna, C. -T. Dinh, O. Voznyy, E. M. Larin, E. Kumacheva and E. H. Sargent, *ACS Catal.*, 2016, **6**, 8115-8120.
- S18. J. K. Nørskov, T. Bligaard, A. Logadottir, J. R. Kitchin, J. G. Chen, S. Pandelov and U. Stimming, *J. Electrochem. Soc.*, 2005, **152**, J23-J26.
- S19. J. E. Pander, M. F. Baruch, and A. B. Bocarsly, *ACS Catal.*, 2016, **6**, 7824-7833.
- S20. Z. Bitar, A. Fecant, E. Trela-Baudot, S. Chardon-Noblat and D. Pasquier, *Appl. Catal. B: Environ.*, 2016, **189**, 172-180.
- S21. Q. Lai, N. Yang, and G. Yuan, *Electrochem. Commun.*, 2017, **83**, 24-27.

- S22.** X. Sun, L. Lu, Q. Zhu, C. Wu, D. Yang, C. Chen and B. Han, *Angew. Chem. Int. Ed.*, 2018, **57**, 2427-2431.
- S23.** Y. Y. Birdja, R. E. Vos, T. A. Wezendonk, L. Jiang, F. Kapteijn, and M. T. M. Koper, *ACS Catal.*, 2018, **8**, 4420-4428.
- S24.** K. Mou, Z. Chen, S. Yao and L. Lium, *Electrochim. Acta*, 2018, **289**, 65-71.
- S25.** Z. Xia, M. Freeman, D. Zhang, B. Yang, L. Lei, Z. Li, and Y. Hou, *ChemElectroChem*, 2018, **5**, 253-259.
- S26.** R. Hegner, L. F. M. Rosa and F. Harnisch, *Appl. Catal. B: Environ.*, 2018, **238**, 546-556.
- S27.** W. Ma, S. Xie, X. G. Zhang, F. Sun, J. Kang, Z. Jiang, Q. Zhang, D. -Y. Wu and Y. Wang, *Nat. Commun.* 2019, **10**, 892.
- S28.** Z. Zhang, F. Ahmad, W. Zhao, W. Yan, W. Zhang, H. Huang, C. Ma and J. Zeng, *Nano Lett.* 2019, **19**, 4029-4034.
- S29.** F. Liang, Y. Yu, W. Zhou, X. Xu and Z. Zhu, *J. Mater. Chem. A*, 2015, **3**, 634-640.
- S30.** Y. Zhu, W. Zhou, Y. Chen, J. Yu, M. Liu and Z. Shao, *Adv. Mater.*, 2015, **27**, 7150-7155.
- S31.** J. Bao, X. Zhang, B. Fan, J. Zhang, M. Zhou, W. Yang, X. Hu, H. Wang, B. Pan and Y. Xie, *Angew. Chem.*, 2015, **127**, 7507-7512.
- S32.** F. Song, K. Schenk and X. Hu, *Energy Environ. Sci.*, 2016, **9**, 473-477.
- S33.** Y. Zhu, W. Zhou, J. Yu, Y. Chen, M. Liu and Z. Shao, *Chem. Mater.*, 2016, **28**, 1691-1697.
- S34.** L. Xu, Q. Jiang, Z. Xiao, X. Li, J. Huo, S. Wang and L. Dai, *Angew. Chem. Int. Ed.*, 2016, **55**, 5277-5281.